

BRIEF COMMUNICATION

OPEN



Mechanistic origins of corrosion protection of aluminum alloys by graphene/polyetherimide nanocomposite coatings

Tiffany E. Sill ^{1,2}, Wasif Zaheer ^{1,2}, Caroline G. Valdes ¹, Victor H. Balcorta ^{1,2}, Lacey Douglas ^{1,2}, Torrick Fletcher Jr ¹, Sarah Steiger ¹, Neil S. Spinner ³, Stanislav V. Verkhoturov ¹, Viswanathan Kalyanaraman ⁴, Nikhil Verghese ⁴, Matt Pharr ⁵, Kapil Sheth ⁴✉, Rachel D. Davidson ^{1,2}✉ and Sarbajit Banerjee ^{1,2}✉

Light-weighting vehicular components through adoption of light-metal structural alloys holds promise for reducing the fuel consumption of internal combustion engine vehicles and increasing the range of battery electric vehicles. However, the alloyed microstructure and surface precipitates of aluminum alloys render these materials susceptible to corrosion under modest excursions from neutral pH. Traditional chromium-based anodic passivation layers are subject to increasingly stringent environmental regulations, whereas options for sacrificial cathodic films are sparse for electropositive metals. While hybrid nanocomposite coatings have shown initial promise, mechanistic underpinnings remain poorly understood. Here, a fully imidized polyetherimide (PEI) resin is utilized as the continuous phase with inclusion of unfunctionalized exfoliated graphite (UFG). A comprehensive investigation of the mechanisms of corrosion protection reveals key fundamental design principles underpinning corrosion inhibition. First, strong interfacial adhesion, which for PEI is facilitated by binding of imide carbonyl moieties to Lewis acidic sites on Al surfaces. Second, the miscibility of ion-impervious nanoscopic UFG fillers and stabilization of a substantial interphase region at UFG/PEI boundaries that result in minimizing the free volume at the filler/polymer interface. Finally, extended tortuosity of ion diffusion pathways imbued by the below-percolation-threshold 2D fillers. These three design principles help govern and modulate ion transport from electrolyte/coating interfaces to the coating/metal interface and are crucial for the extended preservation of barrier properties. The results suggest an approach to systematically activate multiple modes of corrosion inhibition through rational design of hybrid nanocomposite coatings across hard-to-abate sectors where light metal alloys are likely to play an increasingly prominent role.

npj Materials Degradation (2023)7:35; <https://doi.org/10.1038/s41529-023-00349-2>

INTRODUCTION

Corrosion exerts an unrelenting toll on infrastructure and represents an ever-increasing burden on the global economy. By some accounts, depreciation, replacement, and repair traceable to materials degradation costs ca. \$2.5 trillion each year^{1–4}. While the *a priori* design of alloys to mitigate corrosion remains an active area of research, the vast expanse of base metal components used in the built environment, surface and maritime transportation, mineral and hydrocarbon extraction, and defense implies that inhibition and protection will remain the primary strategy for many years to come. Protective coatings play a central role in preservation of corrodible components⁵. However, some of the most effective active elements of protective coatings such as hexavalent chrome and organotin compounds are severely toxic and pose a threat to vulnerable ecosystems and human health^{5–7}. Much recent effort has focused on the corrosion protection of light structural metals and their alloys, which are susceptible to severe degradation at relatively modest excursions from neutral pH⁸. Developing design strategies to protect electropositive light metals (such as alloys of magnesium, aluminum, and calcium) is of pivotal importance to the greater adoption of these materials in vehicular transportation where light-weighting is of urgent importance to reduce fuel consumption and/or increase range. The strongly electropositive nature of these metals implies that the playbook used to protect low alloy steels based on sacrificial

cathodic protection is of limited value. Hybrid polymer nanocomposites hold promise for implementation of alternative corrosion inhibition mechanisms, but their development thus far has been limited by a relatively narrow mechanistic understanding of modes of operation^{5,9–11}. Some intriguing conceptual ideas have emerged that can be broadly classified as active and passive protection. Active corrosion protection involves corrosion inhibition based on engendering specific electrochemical reactivity at the metal surface using corrosion inhibitors or sacrificial inclusions that preferentially corrode prior to the substrate^{5,9,11}. Some recent illustrative developments of active coatings include self-healing coatings that are activated upon development of a physical defect in the coating, such as by releasing an encapsulated monomer^{5,9}. Passive protection mechanisms are physical barriers that slow the overall diffusion rate of corrosive species to the substrate. This type of protection can be realized through control of the coating microstructure (such as through alloying, dealloying, or grain refinement)^{12,13}, surface modification to reduce corrosion nucleation sites⁹, activation of anodic passivation mechanisms, and the design of hybrid nanostructured coatings to elongate ion diffusion pathways^{5,9–11}. In this article, we present the design of a graphene/polyetherimide (PEI) protective coating for aluminum alloys. Through a combination of structural, interfacial, and electrochemical characterization, we distinguish the specific roles

¹Department of Chemistry Texas A&M University, College Station, TX 77842, USA. ²Department of Materials Science and Engineering Texas A&M University, College Station, TX 77842, USA. ³Pine Research Instrumentation Inc., Durham, NC 27705, USA. ⁴SABIC Specialties, Mt. Vernon, Indiana, IN 47620, USA. ⁵Department of Mechanical Engineering Texas A&M University, College Station, TX 77842, USA. ✉email: kapil.sheth@sabic.com; racheldavidson@tamu.edu; banerjee@chem.tamu.edu

of tortuosity, interphase formation, and interfacial interactions in constituting an effective barrier coating.

Light-weighting light- and heavy-duty vehicles is a cornerstone of the energy transition and is imperative to reduce fuel combustion in internal combustion engine vehicles and increase the range of electric vehicles^{8,14}. A substantial global effort has focused on replacement of heavier steels with lightweight high-strength low alloy steels, carbon fiber composites, or light metal alloys of aluminum or magnesium. The design of lightweight structural alloys relies on inclusion of precipitates to achieve the desired load-bearing properties; the heterogeneous composition of such alloys underpins a strong proclivity for galvanic corrosion as a result of the creation of localized anodic and cathodic sites^{15–20}. The corrosion properties of such alloys can be understood considering Pourbaix diagrams of the light-metal components of the alloys as a starting point^{15,21,22}. Strengthening and passivating additives have a deleterious effect on corrosion properties by shrinking passivation windows of alloys as compared to the pure metals^{17,19,21–23}.

Sacrificial coatings are the most conventional mode of corrosion protection. The operational principle of such coatings involves an overlayer of a species higher in the electrochemical series, which thereby serves as an anode, and is preferentially corroded before the underlying substrate. In the case of aluminum alloys, options for more electropositive sacrificial anodes are severely limited. Magnesium is often the metal of choice to imbue cathodic protection but is itself rapidly corroded, and can be exceedingly reactive in challenging environments^{24–27}. An alternative mechanism involves deposition of a less electrochemically active metal, which nevertheless constitutes a dense and conformal passivating layer that is readily transported and precipitated at damage sites as a result of its low solubility oxidation product^{17,28}. This form of protection, anodic passivation, is the primary mode of protection afforded by chromium-based coatings. However, it has been exceedingly challenging to identify sustainable alternatives that are comparable to chromate passivation layers in their ability to passivate damaged areas^{7,15,18,19}.

Nanocomposite coatings are versatile in their design and function, which derives from the myriad choices in selection of the continuous polymeric matrix and embedded fillers. In addition to corrosion protection, hybrid nanocomposites can be used to imbue^{7,11,29} thermal insulation, thermal expansion compensation^{30–34}, abrasion resistance, and to modulate solar heat gain and aesthetic appearance^{35,36}. Exfoliated graphite and layered double hydroxides have been embedded within polymeric matrices to enhance corrosion inhibition wherein they provide barrier protection and enhance the tortuosity of ion diffusion pathways^{11,37,38}. Previous studies based on finite element modeling of transport processes illustrate that the dimensions of graphene sheets do not substantially alter corrosion performance. However, the loading of graphene sheets and the extent of dispersion play a key role in governing the corrosion performance of the coating^{11,39,40}. In particular, phase segregation of graphene and formation of a percolative network deleteriously impact corrosion behavior⁴¹. Above a certain threshold concentration, graphene-based materials can agglomerate to form a percolative network, which accelerates galvanic corrosion across the thickness of the coating^{11,42}. In the case of aluminum alloys, galvanic coupling induces preferential corrosion of the metal substrate based on the differential in open-circuit potential (OCP) of graphite and the underlying substrate¹¹. Preventing the formation of a percolative network, and mitigating phase segregation of conductive particles, becomes increasingly important as the loading of the functional filler is increased^{7,11,15,37,39,43,44}. Polymer chains fill spaces between graphene particles to physically modulate interplatelet contact points and preclude the development of a conductive network. Strategies to modulate this critical “interphase” region in immediate proximity of the functional filler and

its evolution as a function of filler loading and dispersion remains underexplored^{11,39,40,43}.

The interphase region produces a gradation of properties from the polymeric matrix to the hard functional filler. These interactions result in enhanced composite properties such as increased hardness, improved load transfer, greater fracture toughness, reduced predilection for microcrack formation, and enhanced thermal stability^{38–40,43,45}. While the importance of the interphase has become apparent in recent years, mechanistic understanding of corrosion and passivation processes, the role of interphase interactions between graphene and the polymer matrix in corrosion protection, and modes of interfacial interactions at light metal interfaces remain to be elucidated, and have limited the rational design of hybrid nanocomposites for mechanism-informed mitigation of corrosion^{38–40,43}. We examine here the interfacial interactions of a PEI resin that shows strong adhesion to aluminum alloys, decipher the role of an interphase that plays a key role in impeding ion transport, and discuss the origins of large tortuosity enhancements imbued by inclusion of varying loadings of exfoliated unfunctionalized graphite (UFG) in PEI. We decipher the mechanistic origins of corrosion inhibition afforded by UFG/PEI nanocomposites and converge on optimal formulations that yield extended corrosion protection under accelerated testing conditions. The UFG/PEI nanocomposites are benchmarked against alternative commercially available polymers. To the best of our knowledge, this represents the first benchmarked study comparing varying polymer resins with different graphene loadings for corrosion protection of light metal alloys.

RESULTS

Interphases and interfaces

Aluminum alloys such as AA 7075 are characterized by a heterogeneous microstructure, which includes a high density of surface precipitates. While such precipitates are imperative for hardening, they constitute localized anodic and cathodic surface sites (Fig. 1)⁴⁶. As such, galvanic corrosion is readily initiated when surface half cells are connected through a conducting medium. Hybrid nanocomposite coatings prevent direct electrochemical coupling between surface sites by occluding ion transport across the surface. Planar nanoscopic inclusions, oriented horizontally during casting of the films, have active interfaces that can interact with polymer chains leading to the development of the interphase region (Fig. 1b). Such interfacial interactions anchor the interlocking polymer chains to UFG inclusions, resulting in restricted mobility, increased microhardness, and more effective load transfer at the microscale^{39,40,43,45}. Greater microhardness and improved load transfer enhance tortuosity through decreased matrix distortion and by mitigating channel formation under osmotic pressure gradients. Immobilization of polymer chains further reduce matrix relaxation behavior and decrease void space generated from point defects within the graphene sheet. As a result of these interactions, the interphase plays a critical role in enhancing barrier protection by extending the length of ion diffusion pathways, forcing ions to make their way around a maze of logjammed fillers from the liquid interface to the metal surface (Fig. 1a)^{7,11,38,39,44,47,48}. This simplified model points to two key design principles for the framework of effective nanocomposite coatings for corrosion inhibition. The first imperative is strong adhesion of the polymer to the metal surface, hence the surface treatment of substrates to ensure optimal interfacial interactions. Given the Lewis acidic nature of AA 7075 surfaces, a base polymer with a high abundance of Lewis basic binding sites is desirable. Indeed, these principles have guided our selection of PEI as the base resin. Table 1 contrasts the results of ASTM adhesion tests for PEI coatings on AA 7075. For as-prepared films, strong adhesion is observed indicating a strong interaction at the coating/metal

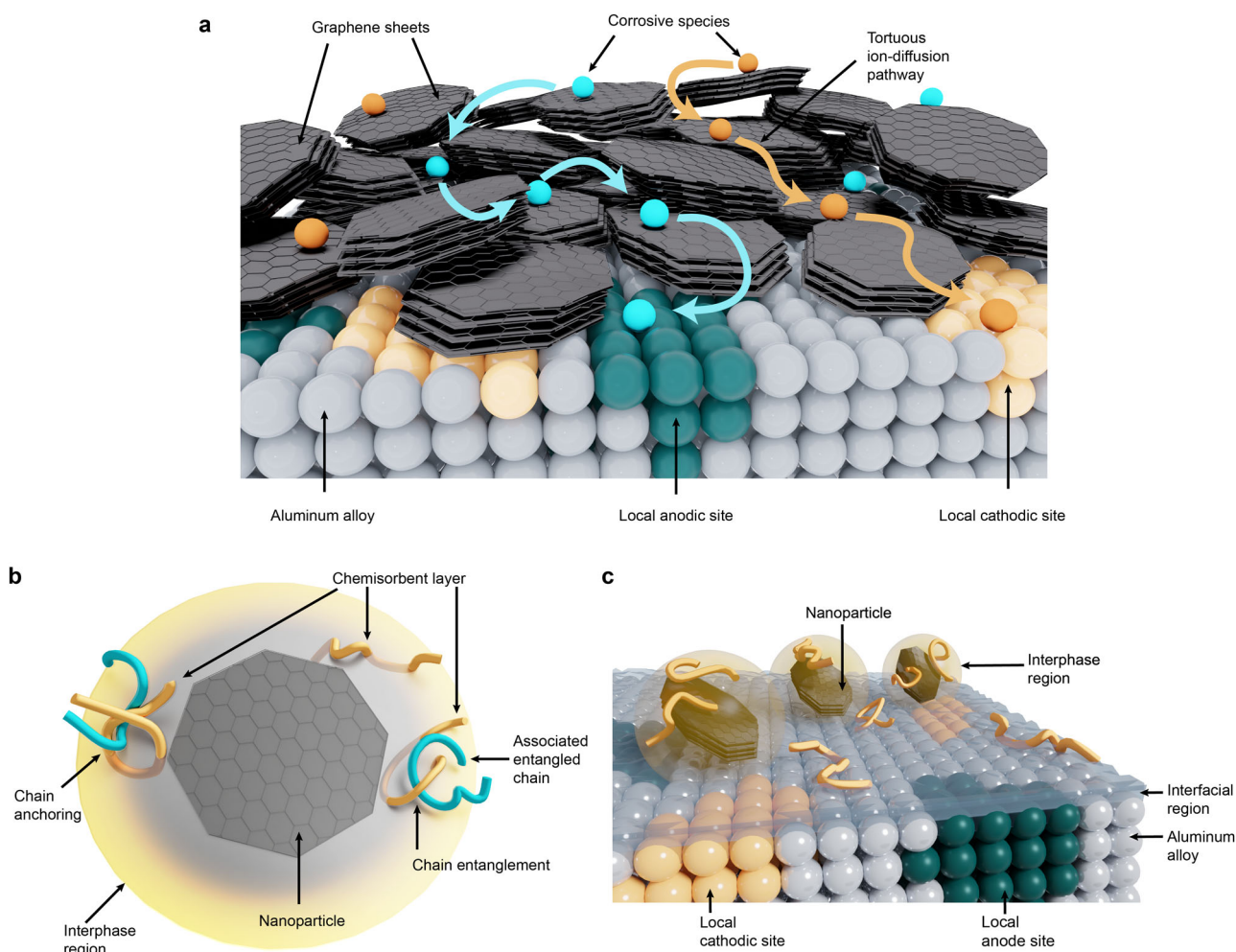


Fig. 1 Interphasal and Interfacial Interactions in UFG/PEI Nanocomposite Coatings on AA 7075 substrates. **a** Schematic illustrating the increased length of ion-diffusion pathways upon embedding of graphene within PEI; **b** a schematic of the interphase region created through inclusions of UFG with the PEI matrix; and **(c)** schematic illustrating interphase and interfacial regions that together form an effective barrier protecting AA 7075 substrates from corrosion.

Table 1. Mechanical Testing and Adhesion Data for PEI and UFG/PEI Coatings on AA 7075.

Sample	nanoindentation elastic modulus (GPa)	nanoindentation hardness (MPa)	ASTM D4541-09 (pull off)	ASTM D3359 (tape)	ASTM D2197-13 (scrape)
PEI	5.07 ± 0.25	410 ± 40	no failure	5B	>10 kg
1 wt.% UFG/PEI	5.50 ± 0.33	443 ± 10	no failure	5B	>10 kg
3 wt.% UFG/PEI	5.48 ± 0.40	426 ± 60	no failure	5B	>10 kg
5 wt.% UFG/PEI	5.53 ± 0.08	418 ± 50	no failure	5B	>10 kg

Nanoindentation and ASTM adhesion testing data for PEI and UFG/PEI coatings on AA 7075.

interface limiting ion penetration and leading to high barrier protection in the coating system. Similarly, the benchmarks exhibit overall strong adhesion properties as shown in Supplementary Table 1; however, as a result of their epoxide and hydroxyl moieties, the epoxy variations are hydrophilic, which leads to extensive water uptake, and ultimately, delamination (*vide infra*). Next, the embedded filler must itself be impervious to water and ions and should, furthermore, interact with the host polymer matrix in a manner that engenders miscibility and precludes stabilization of interfacial conductive voids. For ion- and water-

impermeable UFG fillers with extended π -conjugated frameworks, polymers with conjugated backbones are desirable to foster miscibility through $\pi-\pi$ interactions. Aromatic imides such as PEI have a high density of aromatic rings and are thus expected to form a dense and ion-impermeable interphase as depicted in Fig. 1b^{39,40,44,48}. Interphasal interactions were directly evidenced using nanoindentation.

A summary of the mechanical properties obtained for the coatings are displayed in Table 1 and Table S1. Loading-unloading curves are shown in Supplementary Fig. 2^{49,50}.

Supplementary Fig. 3 shows comparative plots of the microhardness and elastic moduli of the benchmarks and PEI coatings. UFG inclusions are found to produce a crystalline strengthening mechanism, which is suggestive of the development of an interphase region^{51,52}. The 3 wt.% formulation displays the highest variation, indicated by the standard deviation line on the graph, which suggests greater viscoelastic character, and therefore, a more expansive interphase region. The addition of UFG does not significantly impact the Young's modulus of the coating formulations, which is consistent with the low loadings. The elastic moduli measured here are similar to the 5.17 GPa value reported for PEI coatings prepared by in situ imidization of polyamic acid^{11,53}. These results thus attest to the formation of a substantial interphase region around the fillers (Fig. 1b), indicating a strong interaction between the embedded fillers and matrix, which is conducive to achieving homogenous dispersion of UFG in PEI^{29,45,54–56}.

Interfacial interactions between the PEI and AA 7075 substrates have been investigated using ToF-SIMS and XANES. The ToF-SIMS depth profile in Fig. 2a maps the intensity of m/z peaks corresponding to the emitted ion fragment of interest over time across the coating/metal interface. Distinctive C_2H and CNO fragments as well as C_4 and C_3 fragments are derived from PEI and UFG, respectively. A pronounced Al—O signal is observed and increases in intensity at the AA 7075/(UFG/PEI) interface. The prominent Al—O signal is present even when silicon carbide is used as the abrasive layer to remove the oxy-hydroxide passivation layer, which is observable in Supplementary Fig. 1; no Al—N fragments are observed under these ionization conditions. The results suggest that the active binding site in the PEI polymeric chains are the carbonyl or ether oxygen atoms. This is indeed consistent with trends in bond dissociation energies (Al—O bonds have a bond dissociation energy of ca. 512(4) $\text{kJ}\cdot\text{mol}^{-1}$ compared to 297(96) $\text{kJ}\cdot\text{mol}^{-1}$ for Al—N bonds). Al—O bonding is strongly ionic and furthermore is characterized by strong configuration mixing⁵⁷. Studies of interactions of Al_n clusters with small molecules have moreover found a strong preference for Al—O bonding over Al—N bonding with the former mediating the eventual stabilization of Al—O—Al bridges⁵⁸.

Further information on oxygen bonding modes has been derived from C and O K-edge XANES spectroscopy (Fig. 2b and c). The oxygen K-edge signatures for ethereal and carbonyl oxygens are starkly different owing to the π -bonded nature of the latter⁵⁹. Considering the O K-edge spectrum of the PEI (Fig. 2b), a broad shoulder present at ca. 533 eV can be ascribed to pre-edge transitions from an imide carbonyl^{59–61}. The most prominent $1s\rightarrow\sigma^*$ resonance comprises two features, the more intense imide carbonyl absorption at ca. 537.7 eV and an ether absorption at ca. 539.4 eV^{59–63}. The aluminum oxide control is characterized by a sharp $1s\rightarrow\pi^*$ absorption at ca. 532.4 eV and a $1s\rightarrow\sigma^*$ feature, which is split into a shoulder at ca. 538.5 eV as a result of O—H bonds from structural waters of hydration and an absorption feature at ca. 541.3 eV, which corresponds to bridging oxygen atoms in the Al_2O_3 structure⁶⁰. A sample interfacing PEI with Al flakes shows the sharp $1s\rightarrow\pi^*$ aluminum oxide signal at ca. 532.4 eV⁶⁰. Additionally, two distinct features can be distinguished within the broad absorption: the carbonyl absorption at ca. 537.6 eV is reduced in relative intensity as compared to as-cast PEI. This indicates that the imide carbonyl oxygen binds to surface Lewis acidic aluminum sites through the formation of C—O—Al bridging linkages. This binding mechanism is further corroborated by the increased relative intensity of the ca. 540.2 eV absorption, which arises from ether-like bridging oxygen modes. The preferential binding of imide carbonyls to surface Lewis acidic sites is furthermore consistent with the higher basicity (lower pK_b) of carbonyl groups as compared to ether groups.

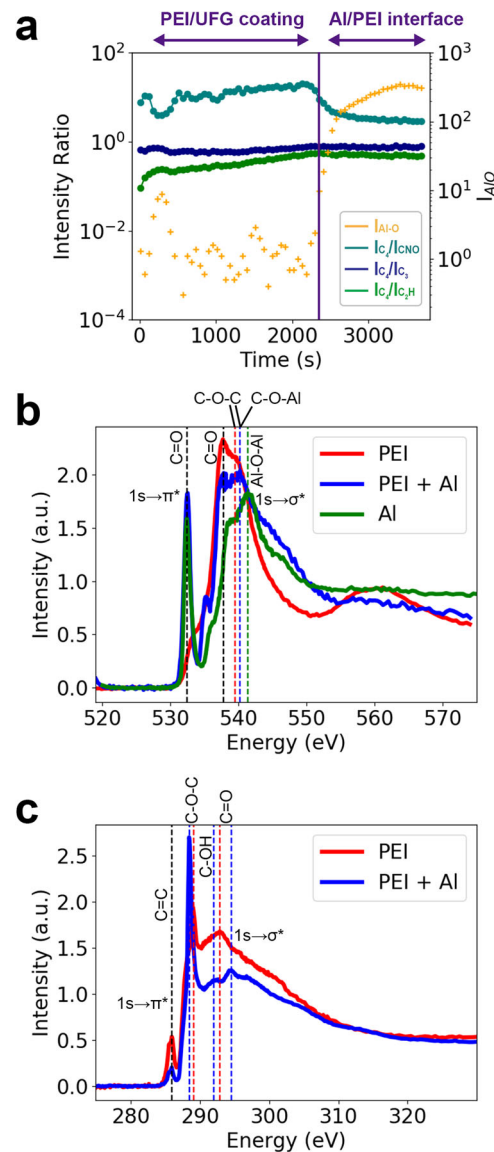


Fig. 2 Investigation of Interfacial Interactions Between UFG/PEI Nanocomposite Coatings and AA 7075 Substrates. **a** ToF-SIMS depth profile illuminating strong Al—O signals at the metal/coating interface; XANES spectra acquired at **(b)** oxygen and **(c)** carbon K-edges for PEI, PEI interfaced with Al flakes, and the Al flakes to investigate the binding mechanisms between the PEI and aluminum substrate. Peak assignments are noted in the spectra and are further discussed in the text.

Carbon K-edge XANES spectra are plotted in Fig. 2c. Both the PEI and PEI/Al sample exhibit $1s\rightarrow\pi^*$ ($\text{C}=\text{C}$ bond) absorption features derived from π -bonded carbon atoms at ca. 285.9 eV^{62,64,65}. This feature is decreased in intensity upon binding to Al surfaces as a result of the carbonyl group being transformed to a σ -bonded bridging linkage. The C K-edge $1s\rightarrow\sigma^*$ feature is characterized by a sharp absorption that is shifted from ca. 289.0 eV in PEI to ca. 288.4 eV upon interfacing with Al; the observed red shift is consistent with weakening of the carbonyl C—O bond; the concomitant enhancement in intensity suggests electron depletion and a greater density of unfilled states, which is furthermore consistent with interactions with a Lewis acidic site^{61,62}. The shoulder observed at ca. 291.9 eV arises from the $1s\rightarrow\sigma^*$ transition of C—OH structural waters of hydration present in the aluminum oxy-hydroxide passivation layer in the

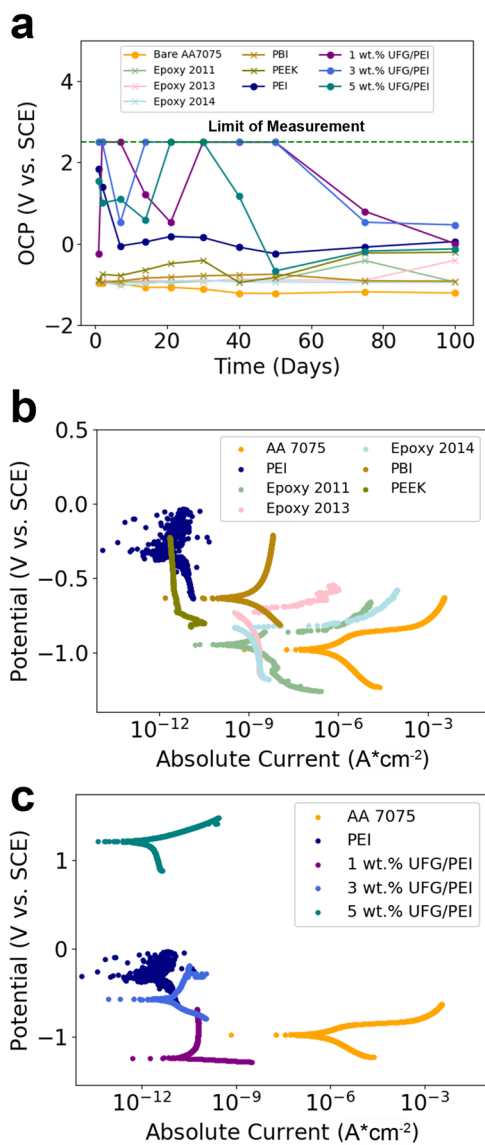


Fig. 3 OCP and Tafel Analysis of Coated Substrates. **a** Evolution of OCP measured 100 days for abraded AA 7075, five benchmark polymeric coatings, and four PEI and UFG/PEI coatings. The coated substrates have been immersed in 3.5 wt.% aqueous NaCl solutions under ambient conditions. **b** Tafel plot of AA 7075, three epoxy formulations, PEEK, PEI, and as-cast PEI. **c** Tafel plot of as-cast PEI, and 1, 3, and 5 wt.% UFG/PEI formulations.

sample^{59,64}. Taken together, the TOF-SIMS and XANES data point to strong interfacial adhesion of PEI to freshly prepared AA 7075 surfaces mediated primarily by interactions of imide carbonyl oxygens with Lewis acidic surface sites. The strong interfacial interactions underpin the strong adhesion of PEI to AA 7075 and serve to passivate surface cathodic and anodic sites, which leads to the exceptional corrosion protection afforded to the underlying substrate.

Electrochemical processes and mechanisms of corrosion protection

OCP values have been monitored for bare and coated substrates immersed in 3.5 wt.% aqueous solutions of NaCl for 100 days (Fig. 3a) to monitor the corrosion potential. The coated substrate serves as the working electrode in a three-electrode system¹¹. The

AA 7075 substrate exhibits the lowest corrosion potential at -0.96 V versus SCE, which indicates the presence of active corrosion processes in the system, leading to the continuous breakdown of the passive oxyhydroxide layer as a result of charge-transfer redox events initiated by chloride ions in the electrolyte²⁸. The five benchmark polymer-coated substrates are at slightly higher potentials as compared to abraded AA 7075. As-cast PEI starts with a higher initial OCP of $+1.8$ V vs. SCE but drops to -0.05 V vs. SCE within 7 days and continues to straddle voltages between -0.25 V and $+0.25$ V for the remainder of the 100 days. This represents the highest value of unfilled polymer coatings evaluated in this work and attests to the strong interfacial adhesion of PEI to the substrate, which endows desired barrier properties. The OCP of the UFG/PEI formulations are initially beyond the range of detection owing to the high capacitance of the coating; only beyond 75 days can the OCP values be measured. Coating capacitance is directly related to the dielectric properties of organic films; hence, water uptake gives rise to variations in coating capacitance values. Once a sufficient amount of water has permeated into the coating, the capacitance values are decreased such that the OCP is shifted within the detectable range of the instrument^{66,67}. The large observed variation of OCP values for the UFG/PEI coatings indicates a slower diffusion rate of water into the nanocomposites as compared to the pristine PEI film. The 1 and 3 wt.% UFG/PEI nanocomposite coatings maintain high OCPs, substantially greater than the bare substrate and other coatings, which suggests formation of a passivation layer with increased barrier properties. In contrast, the 5 wt.% UFG/PEI coating has an OCP above the other benchmarks but below as-cast PEI. The relative decrease of the OCP is attributable to the high UFG concentration, which stabilizes a percolative network, increases the rate of water uptake, and gives rise to galvanic corrosion^{11,37}.

PDP and Tafel analysis have been performed using a three-electrode cell with the coated substrate as the working electrode⁶⁸ to extract the corrosion current density (I_{corr}) and Tafel constants (b_a , b_c)¹⁵. Tafel analysis of the benchmark polymers and nanocomposite coatings are contrasted in Fig. 3b. The bare AA 7075 substrate shows the highest corrosion current density of $4.17 \times 10^{-6} \text{ A} \cdot \text{cm}^{-2}$. The extended linear region at higher potentials measured for AA 7075 indicates a moderate passivation region in the anodic direction, followed subsequently by pit nucleation and propagation, which is manifested in PDP plots as a sharp increase in corrosion current density¹⁵. Substrates with benchmark polymer coatings exhibit I_{corr} values of $1.57 \times 10^{-8} \text{ A} \cdot \text{cm}^{-2}$ or lower. The three epoxy formulations exhibit a shallow passive region. In these substrates, pit nucleation and propagation are initiated almost immediately during anodic sweep. In contrast, anodic sweeps of PEEK- and PBI-coated substrates plateau at potentials more positive than the corrosion potential, indicating extended passivation and relatively better barrier protection. Figure 3c contrasts AA 7075 with PEI- and UFG/PEI-nanocomposite-coated substrates, which exhibit still lower I_{corr} values, more than two orders of magnitude lower than the benchmark polymers ($<1.17 \times 10^{-10} \text{ A} \cdot \text{cm}^{-2}$). The shape of the anodic curves are suggestive of an extended passivation region for all but the 5 wt.% UFG/PEI-coated substrate; this substrate does not exhibit a passivation region, which indicates that galvanic cell formation and pit nucleation is initiated immediately upon anodic sweep. The 1 and 3 wt.% UFG/PEI systems thus again demonstrate the most promise for extended passivation regimes.

In order to examine the dynamical evolution of electrochemical processes upon extended immersion in brine solution, electrochemical impedance spectroscopy has been performed for bare and coated substrates. The bare AA 7075 will be discussed first to establish a baseline for performance evaluation followed by a representative selection of benchmarks including epoxy variations, PEEK, and PBI; a more extensive discussion of benchmarks is

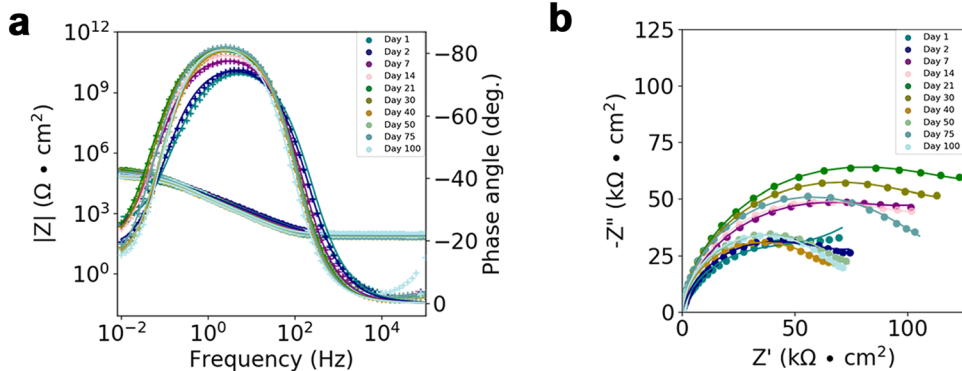


Fig. 4 Plots Depicting the Evolution of EIS for Bare AA 7075. Bode (a) and Nyquist (b) plots for AA 7075 for a 100 day exposure to an aqueous solution of 3.5 wt.% NaCl.

included in the Supporting Information. PEEK is directly contrasted to PEI with regards to functional performance, whereas another comparable resin PBI is discussed in the Supporting Information. We devote most of our attention to as-cast PEI, a 3 wt.% UFG/PEI that exhibits optimal performance, and 1 and 5 wt.% UFG/PEI formulations as systematic variations to examine the role of tortuosity derived from UFG incorporation.

Figure 4 shows Bode and Nyquist plots for the abraded AA 7075 substrate exposed to a 3.5 wt.% aqueous solution of NaCl over the course of 100 days. Figure 4a shows the magnitude of the impedance at the lowest frequency, $|Z|_{0.01\text{ Hz}}$, which indicates that the overall resistance of the system is around $10^5\text{ }\Omega\text{-cm}^2$. Two time-constants are discernible in Fig. 4a, the capacitive response in the 10^3 – 10^1 Hz region is ascribed to charge-transfer processes at the metal/electrolyte interface, whereas the beginning of a plateau in the inductive region at 10^{-1} – 10^{-2} Hz corresponds to the deposition of corrosion products at the metal/electrolyte interface. The evolution of equivalent circuit models computed from this data is shown in Supplementary Fig. 4 and further discussed in Supplementary Table 2. The impedance response of bare AA 7075 is modeled with a single time constant for days 0–75 (Supplementary Fig. 4a), then evolves to two time constants (Supplementary Fig. 4b)^{69,70}. The Nyquist plot in Fig. 4b shows the presence of a capacitive loop across the entire range of frequencies, which indicates the formation of a passivation layer as a result of charge transfer events at the metal/electrolyte interface. A short diffusion tail is observed to emerge at 75 days and is ascribed to the adsorption of intermediate species onto the passive oxyhydroxide film, which serves as a passivating layer and limits the rate of diffusion of corrosive species to the substrate^{15,71}. The measured baseline behavior of AA 7075 sets the stage for comparisons of coating performance across the different benchmark polymer and nanocomposite coatings.

In addition to monitoring the AC impedance response upon salt-water immersion for 100 days, the recovered samples have been examined by cross-sectional scanning electron microscopy (SEM) and energy-dispersive X-ray spectroscopy (EDX) elemental mapping to examine the fate of coating/metal interfaces at the end of the exposure period. Figure 5 compares the performance of a commercial epoxy variation with no fillers (epoxy 2011), PEEK PEI, and 3 wt.% UFG/PEI coatings. We first begin by examining an unfilled epoxy coating as it demonstrates the greatest evidence for corrosion under the exposure conditions. Figures 5b and 5f show extensive pitting at the epoxy/metal interface upon 100 days of exposure. The Bode plot for the epoxy-coated substrate (Fig. 5j) exhibits a $|Z|_{0.01\text{ Hz}}$ value of around $10^6\text{ }\Omega\text{-cm}^2$, which is only an order of magnitude higher than the abraded AA 7075 substrate. This value drops by an order of magnitude at the end of 100 days, indicating delamination and almost complete loss of protection. The corresponding Nyquist plot (Fig. 5n) exhibits a capacitive loop

corresponding to charge transfer events, a diffusion tail indicative of diffusion-limitations to corrosion kinetics, and an induction loop that suggests that intermediate species adsorbed during the charge transfer process dissolve the passivating layer and induce pit nucleation and propagation.

Charge transfer events can take place sequentially—these are modeled as a series of Randle's cells (see for example, the equivalent circuit model for a PEEK-coated substrate in Supplementary Fig. 5e). Alternatively, charge transfer events can also take place simultaneously, for instance, when water and corrosive species penetrate the coating, and a pit is nucleated at the metal surface. In this scenario, corrosion products can be deposited at the same time whilst corrosive species continue to permeate across the film. The embedded model in Supplementary Fig. 5a represents simultaneous corrosion events. Extensive water uptake in epoxy formulations requires complex equivalent circuit models to fit the impedance response (Supplementary Fig. 6 and Supplementary Table 3)⁷². Supplementary Fig. 7 demonstrates EIS and cross-sectional SEM/EDX data for the other two epoxy variations, which are also characterized by extensive water absorption, delamination, and pitting corrosion. Supplementary Fig. 8, Supplementary Fig. 9, and Supplementary Table 3 characterize the evolution of the equivalent circuit models demonstrating a complex convolution of water uptake, charge transfer, electrochemical double layer formation, pit nucleation, and pit propagation.

Hygroscopic PBI³² shows similar behavior to the epoxy formulations including delamination and coating failure (Supplementary Fig. 7). The Nyquist plots in Supplementary Fig. 7 demonstrate some key differences for PBI-coated substrates as compared to the epoxy coatings detailed in the SI. Nevertheless, in the case of the PBI coatings, the trapped corrosion products are unable to inhibit pit formation and propagation at the metal surface (Supplementary Fig. 10 and Supplementary Table 3).

Figure 5a–d show SEM images and associated EDX maps (Fig. 5e–h). Figure 5a reveals that PEEK is delaminated from the substrate in localized areas upon immersion for 100 days in salt solution, allowing ingress of water and corrosive species in pockets between the film and the substrate. Corrosion products precipitated at the metal/electrolyte interface form a passive aluminum oxyhydroxide layer, which is seen as the migration of Al out of the substrate into the interface (Fig. 5e). Aluminum migration can manifest in the form of surface precipitates, such as in the case of PEEK-coated substrates, or alternatively, corroded and mobilized aluminum species are dissolved into the electrolyte solution (313 ng·mL^{−1} of Al has been measured for the PEI-coated substrate after 100 days of exposure using inductively coupled plasma mass spectrometry measurements). The Bode plot for the PEEK-coated substrate (Fig. 5i) is characterized (shown in Supplementary Fig. 5) by two time-constants for the first 21 days;

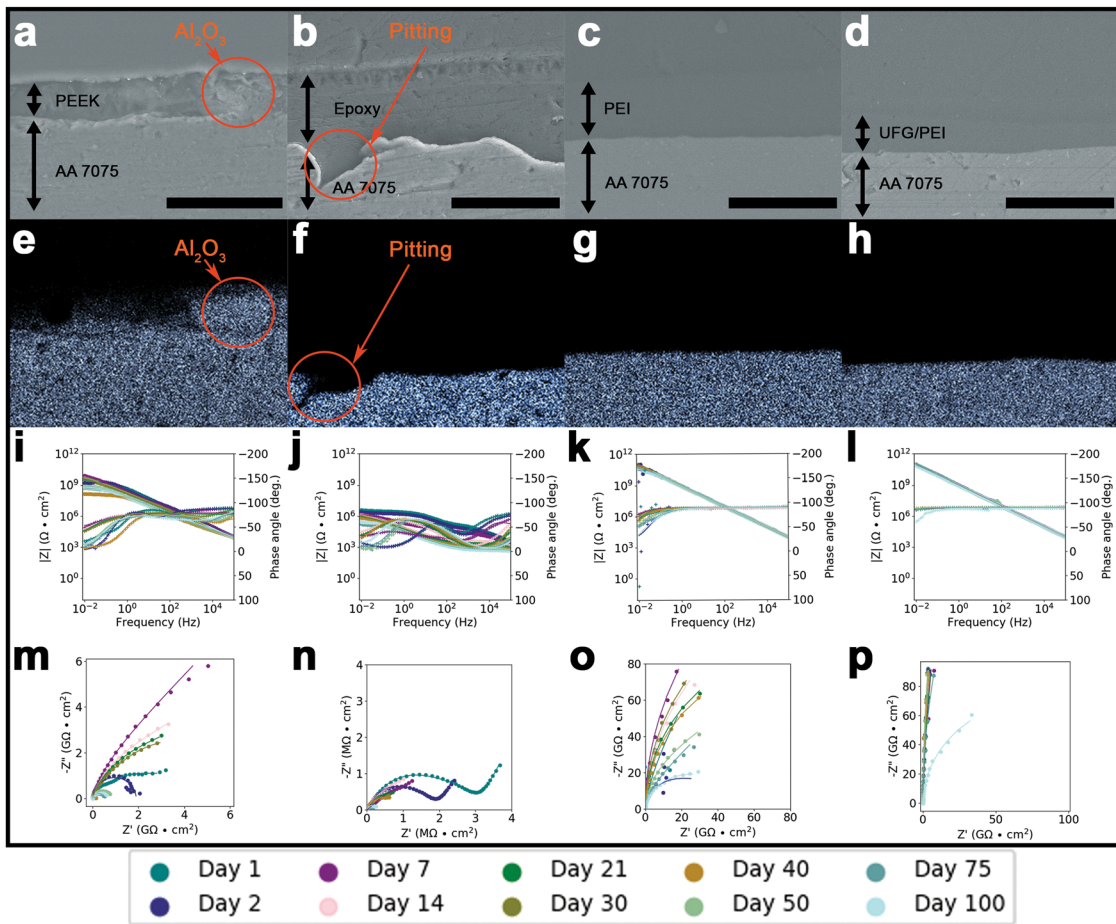


Fig. 5 Electrochemical processes, interface characterization, and corrosion mechanisms in coated AA 7075 substrates. Post-exposure SEM cross-sectional views of coatings comprising (a) PEEK, (b) epoxy (2011) variation with no fillers, (c) PEI, and (d) 3 wt.% UFG/PEI, respectively with the scale bars measuring 50 μm distance, on AA 7075 substrates monitored across 100 days of exposure to 3.5 wt.% aqueous solutions of NaCl. Aluminum EDX maps of coatings comprising (e) PEEK, (f) epoxy, (g) PEI, and (h) 3 wt.% UFG/PEI. Bode plots corresponding to coatings comprising (i) PEEK, (j) epoxy, (k) PEI, and (l) 3 wt.% UFG/PEI. Nyquist plots for coatings comprising (m) PEEK, (n) epoxy variation, (o) PEI, and (p) 3 wt.% UFG/PEI monitored across 100 days of exposure to 3.5 wt.% aqueous solutions of NaCl.

a third time constant emerges thereafter, and is indicative of the formation of additional corrosion sites at the metal/coating interface, which is consistent with the transport of Al from the bulk to the interface observed in SEM and EDX analysis. The overall impedance at the lowest measured frequency, $|Z|_{0.01 \text{ Hz}}$, of PEEK starts at around $10^9 \Omega\cdot\text{cm}^2$ and is generally maintained over the course of the 100 day study (Supplementary Table 3)^{73,74}. The corresponding Nyquist plot, Fig. 5m, shows a capacitive loop, which based on cross-sectional SEM imaging, is ascribed to passivation at the metal/coating interface. The results suggest that the electrolyte solution diffuses through the coating and reaches the bare substrate between days 21–30 when the third time constant becomes prominent as a passivation layer is formed.

Figures 5c and 5d show the smooth interface between PEI and 3 wt.% UFG/PEI coatings and the AA 7075 substrate after 100 days of salt-water immersion. Additionally, no aluminum migration is discernible in the EDX maps in Fig. 5g and 5h, indicating preservation of the interface discussed in the preceding section. Bode plots (Figs. 5k and 5l) demonstrate a single time constant for PEI- and UFG/PEI-coated substrates through day 75 exhibited in the circuit model in Supplementary Fig. 11a. The appearance of a second time constant in the PEI-based coatings beyond 75 days indicates eventual ingress of corrosive species (Supplementary Fig. 11b, described in Supplementary Table 2). These findings suggest that appropriately cast PEI coatings afford high barrier protection, which can protect an underlying substrate for at least 75 days

under ambient conditions. The Bode plots for the unfilled PEI-coated substrate (Fig. 5k) and the 3 wt.% UFG/PEI nanocomposite coating (Fig. 5l) exhibit an initial $|Z|_{0.01 \text{ Hz}}$ value of ca. $10^{11} \Omega\cdot\text{cm}^2$, which is maintained for the duration of the study. The Nyquist plot in Fig. 5o indicates a capacitive loop, which is attributable to barrier properties and passivation afforded by PEI. Figure 5p, the Nyquist plot for the 3 wt.% UFG/PEI-coated substrate furthermore indicates near-ideal capacitive behavior; a capacitive loop manifests near the end of the exposure period, suggesting that ionic species diffused through the coating and reached the substrate between days 75–100. A beneficial passive oxyhydroxide layer is stabilized, as represented by the equivalent circuit model in Supplementary Fig. 12b (see also Supplementary Table 2). The aluminum oxide corrosion products are trapped at the metal/coating interface, where they are incorporated within the passivation layer. These results attest to the superior performance of UFG/PEI coatings as compared to PEI alone, which is traceable to increased tortuosity and ion transport resistance afforded by the UFG inclusions as further evidenced below. The 1 wt.% UFG/PEI coating exhibited similar performance to its 3 wt.% UFG/PEI counterpart; however, the tortuosity enhancement is more modest. Intriguingly, the 5 wt.% UFG/PEI coating saw an even larger decrease (Supplementary Fig. 13) in performance over the course of the 100 days owing to formation of a percolative network that is conducive to inducing galvanic corrosion, as further detailed in the SI. As such, UFG loadings below the

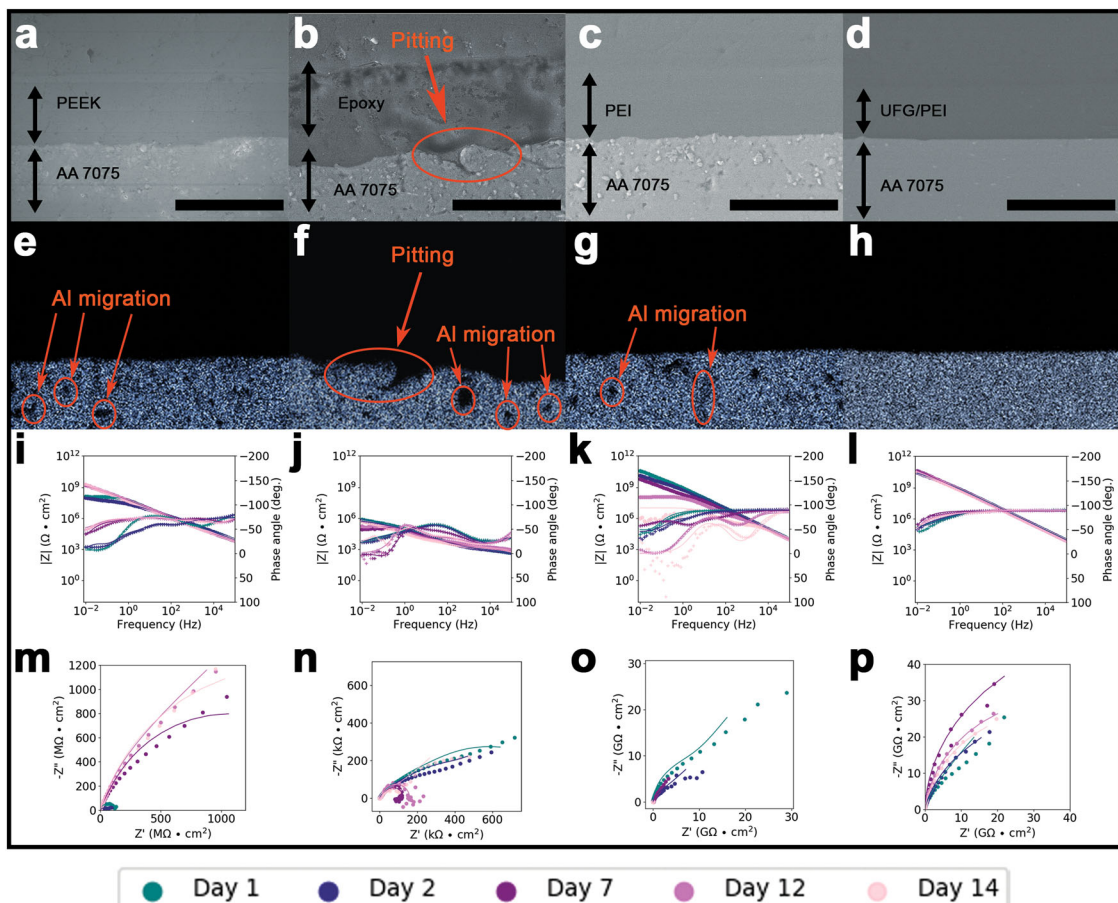


Fig. 6 Electrochemical processes, interface characterization, and corrosion mechanisms upon exposure to salt water at elevated temperature. Post-exposure SEM cross-sectional views of coatings, with scale bars equal to 50 μm , comprising (a) PEEK, (b) epoxy (2011) variation with no fillers, (c) PEI, and (d) 3 wt.% UFG/PEI, respectively, coated onto AA 7075 substrates after exposure for 14 days to a 3.5 wt.% aqueous solution of NaCl at 70 °C. Aluminum EDX maps of substrates coated with (e) PEEK, (f) epoxy, (g) PEI, and (h) 3 wt.% UFG/PEI. Bode plots monitored over 14 days of exposure corresponding to coatings comprising (i) PEEK, (j) epoxy, (k) PEI, and (l) 3 wt.% UFG/PEI. Nyquist plots for (m) PEEK, (n) epoxy variation, (o) PEI, and (p) 3 wt.% UFG/PEI. Nyquist plots for (m) PEEK, (n) epoxy variation, (o) PEI, and (p) 3 wt.% UFG/PEI.

percolative threshold are optimal for enhancing tortuosity without triggering galvanic corrosion^{11,37,39,44,48}. Quantification of tortuosity from electrochemical impedance spectra is precluded by the low free volume and porosity of these systems, which renders conventional transmission line modeling rather challenging. Finite element modeling of variably sized UFG in a continuous polymer matrix has determined normalized diffusivity values, which are inversely proportional to effective tortuosity, to decrease from 0.89 ± 0.02 to 0.79 ± 0.05 and then to 0.71 ± 0.08 upon increasing the UFG loading from 5 to 10 to 17 wt.%, providing a measure of the inhibition of diffusive transport upon incorporating of nanoscopic inclusions¹¹.

Further differentiation in coating performance has been observed under harsher exposure conditions. Coatings were immersed in a 3.5 wt.% aqueous NaCl solution and maintained at 70 °C for 14 days. Comparative SEM, EDX, and EIS data paralleling Fig. 5 is shown in Fig. 6 under these more aggressive conditions. We discuss representative benchmark coatings here, whereas a more complete set is discussed in the Supporting Information.

SEM images of the epoxy (2011) coating (Fig. 6b) upon exposure to salt water under high-temperature conditions shows extensive pitting corrosion and water uptake, which is further corroborated by the EDX map in Fig. 6f. Extensive aluminum migration and voids in the underlying AA 7075 substrate are observed. It is important to note that there are white silicon

contaminants present in the SEM micrographs that are artifacts of the polishing process. These silicon particles appear as holes in the corresponding EDX maps but do not signify aluminum migration in the underlying substrate. The Bode plot in Fig. 6j shows a slow decline in the overall impedance at $|Z|_{0.01 \text{ Hz}}$ by an order of magnitude over the course of 14 days. Additionally, multiple time constants present in the system indicate repeated dissolution and reformation of the oxyhydroxide layer, which initiates pit nucleation and propagation at the coating/metal interface (Supplementary Fig. 14 and Supplementary Table 4). The corresponding Nyquist plot in Fig. 6n, indicates induction loops, diffusion tails, and passivation events in the form of capacitive loops present in the system. The other two epoxy variations exhibit similar modes of failure described in Supplementary Figs. 15 and 16, and Supplementary Table 4.

After 14 days of high-temperature exposure, the PEEK coating is observed to be substantially thicker than the original 20–30 μm thickness as a result of water uptake (Fig. 6a). In addition, Fig. 6e shows clear evidence for aluminum migration, which is manifested by the presence of voids in the underlying AA 7075 substrate. Bode (Fig. 6i) and Nyquist (Fig. 6m) plots for the PEEK-coated substrate show that the overall impedance at $|Z|_{0.01 \text{ Hz}}$ starts around $10^9 \Omega\text{-cm}^2$ and is maintained throughout the 14 day period. However, multiple time constants are observed (modeled in Supplementary Fig. 17 and described in Supplementary Table 4). The capacitive loops show passivation, whereas an inductive

feature emerges prior to day 7, and is correlated with water uptake in the film. PBI shows similar performance to PEEK as observed in Supplementary Fig. 18.

We next consider the PEI and UFG/PEI nanocomposite coatings. The SEM image in Fig. 6c shows water uptake in the as-cast PEI-coated substrate upon high-temperature exposure to salt-water; distinctive voids are visible in the AA 7075 substrate in the EDX map (Fig. 6g). Supplementary Figs. 19d and 19e show corresponding SEM images of 1 and 5 wt.% UFG/PEI-coated substrates, respectively; Supplementary Figs. 19i and 19j exhibit their corresponding EDX maps. Al migration away from the coating/metal interface is observed as a result of accelerated ion transport through imperfections in the coating. The associated Bode plot for as-cast PEI (Fig. 6k), shows a rapid decrease, of the overall impedance by roughly three orders of magnitude from an initial $|Z|_{0.01\text{ Hz}}$ of $10^{11}\Omega\cdot\text{cm}^2$ to $|Z|_{0.01\text{ Hz}}$ of ca. $10^8\Omega\cdot\text{cm}^2$ by day 12, and an additional drastic reduction by another three orders of magnitude to $|Z|_{0.01\text{ Hz}}$ of ca. $10^5\Omega\cdot\text{cm}^2$ by day 14. This is accompanied by the emergence of additional time constants corresponding to coating delamination and additional corrosion events demonstrated by the evolution of the circuit models in Supplementary Fig. 20. The Nyquist plots associated with as-cast PEI (Fig. 6o), and 1 and 5 wt.% UFG/PEI coating (Supplementary Fig. 19s and 19t, respectively) illustrate a capacitive loop and diffusion tails, which suggests delamination of the coatings and the formation of a passivation layer at the alloy/coating interface. The evolution of the equivalent circuit models for 1 and 5 wt.% UFG/PEI are shown in Supplementary Figs. 21 and 22, respectively, and distinguished further in Supplementary Table 5.

The 3 wt.% UFG/PEI-coated substrates are found to withstand even these harsh conditions and show the most optimal ability to withstand corrosion of the samples examined here. The smooth, featureless cross-sectional SEM image (Fig. 6d), and corresponding aluminum EDX map (Fig. 6h) attests to retention of coating integrity even upon high-temperature exposure to salt water. Concurrently, the Bode plot shows no deviation from the overall impedance of $10^{11}\Omega\cdot\text{cm}^2$ and the presence of only a singular time constant; the Nyquist plot (Fig. 6p) indicates an extensive capacitive loop attesting to the impervious barrier properties of the coating. This is demonstrated in the equivalent circuit models shown in Supplementary Fig. 23. The dielectric properties of the coating slow the rate of diffusion of corrosive species through the continuous polymeric matrix. The extended protection offered by the nanocomposite as compared to PEI alone indicates the role of enhanced tortuosity imbued by graphene incorporation and the role of the interphase in enhancing barrier protection afforded by the nanocomposite system as discussed in Fig. 1.

DISCUSSION

Using a suite of structural, interfacial, and electrochemical methods, we have systematically examined the mechanisms by which different polymeric and nanocomposite systems inhibit the corrosion of a light-weight aluminum alloy. We contrast the performance of PEI coatings with and without UFG inclusions with a variety of commercially available polymers, including PBI, PEEK, and three epoxy variations. Through systematic evaluation of corrosion inhibition over the course of 100 days immersion in a 3.5 wt.% aqueous solution of NaCl at ambient temperature, as well as under harsher exposure conditions of 14 days immersion in a 3.5 wt.% aqueous NaCl solution at 70 °C, we have identified key design principles for constructing nanocomposite coatings to inhibit corrosion of light metal alloys and have used this mechanism-informed approach to converge on an optimal nanocomposite coating. The results attest to the importance of (a) strong interfacial adhesion, which in the case of PEI is facilitated by binding of imide carbonyl moieties to Lewis acidic sites on the surface; (b) miscibility of ion-impervious nanoscopic

2D fillers and stabilization of a substantial interphase region, which is enabled by $\pi-\pi$ interactions in graphene/aromatic imide systems, minimizes free volume at the filler/polymer interface, inhibits matrix deformation that leads to channel formation, and impedes ion transport; and (c) extended tortuosity endowed by the below-percolation-threshold concentration of 2D material fillers, which greatly inhibits ion transport from the electrolyte interface to the substrate (Fig. 1a). Notably, at high UFG concentrations, formation of a percolative network drives deleterious galvanic corrosion. A 3 wt.% UFG/PEI nanocomposite coating exhibits the highest performance under both long-term salt-water exposure under ambient conditions, as well as under harsher high-temperature conditions. The coating demonstrates a high overall impedance value of $|Z|_{0.01\text{ Hz}}$ of ca. $10^{11}\Omega\cdot\text{cm}^2$, which is preserved across the duration of exposure, thus indicating desired barrier properties derived from extended tortuosity and a substantial interphase. The formation of the interphase and its ability to decrease matrix distortion and mitigate channel formation under osmotic pressure gradients is further corroborated by nanoindentation measurements. In contrast to the nanocomposite aromatic-imide-based coatings, epoxy, PBI, and PEEK coatings show substantial water uptake, delamination, and void formation with repeated cycles of local passivation, initiation of pitting at new sites, and pit propagation. The results demonstrate the role of interactions across multiple interfaces, graphene/PEI and Al/PEI, in limiting ion transport and surface electrochemical reactions, enabling passivation, and endowing long-term corrosion protection. A notable limitation is the inability to quantify changes in tortuosity. Current models that use impedance data to quantify tortuosity, such as the generalized transmission line method, require a porous microstructure and are not suitable for dense non-porous media such as the composites with low free volumes under consideration⁷⁵. However, finite element modeling results demonstrate substantial tortuosity-dependent inhibition of diffusive transport as a function of particle loading¹¹. Future studies will explore selective pre-passivation of specific cathodic and anodic sites, molecular-weight dependence of segmental interactions and accessible free volume in the coatings, and the embedding of additional fillers to endow multimodal functionality.

METHODS

Synthesis of UFG

UFG was synthesized as described previous work¹¹ by adding 5.0001 g of Bay Carbon SP-1 graphite powder to 100 mL of *N*-methyl-2-pyrrolidone (NMP, Honeywell Research Chemicals) to yield a 4.76 wt.% dispersion. The dispersion was then placed in a Branson 5510 ultrasonicator for 8 h to facilitate exfoliation; the vessel was mechanically agitated every hour to prevent sedimentation of the larger particles.

Size distribution analysis of UFG

Size distribution analyses were performed using scanning electron microscopy (SEM) on a FEI Quanta 600 FE-SEM and atomic force microscopy (AFM) on a Bruker Dimension Icon AFM. The details of SEM imaging are described below. The AFM was completed on tapping mode with a MikroMasch HQ:NSC35 *n*-type silicon tip that had an 8 nm radius, 40° tip cone angle, a force constant of $\sim 16\text{ N}\cdot\text{m}^{-1}$, and a resonance frequency of 300 kHz. Images were analyzed on NanoScope Analysis 2.0 software.

Preparation of UFG/PEI dispersions

Fully imidized polyetherimide, ULTEM 1000 pellets provided by SABIC, were dissolved at a concentration of 10 wt.% in NMP. The UFG dispersion was then added to the dissolved polymer solution

along with additional NMP to obtain UFG loadings of 1, 3, and 5 wt.% in the PEI resin. A loading of 5.9 wt.% of polymer in NMP solution was found to be optimal for spray coating. All dispersions were stored under a headspace of nitrogen to prevent water adsorption.

AA 7075 substrate preparation

Aluminum clad alloy AA 7075 T6 purchased from Bralco Metals was cut into 10 cm × 10 cm squares. One side was abraded with P100 grit sandpaper to remove the outer aluminum oxide passive layer. Substrates were then washed with hexanes (UN1208, Fisher Chemical) to remove packing grease and oils. Next, the substrates were rinsed with acetone (UN1090, Fisher Chemical) to remove water from surface. The surface treatment of the substrates serves two purposes: (1) to allow the PEI to adhere directly to aluminum metal rather than the aluminum oxide passive layer, thereby creating stronger interfacial interactions that increase adhesion, and (2) remove any contaminants such as packing grease and dyes from the surface of the metal.

Automatic spray coating machine

A Specialty Coating Systems Precisioncoat V automatic spray coating machine retrofitted with a hotplate was used to spray coat the substrates. The coating system enables control and optimization of the following parameters: rate of deposition, droplet size, rate of solvent evaporation, the radius of the spray cone, particle acceleration, and substrate impact. As such, the automatic spray coater provides control over the conformity, homogeneity, density, thickness, adhesion, hardness, and microstructure of the coating, enabling mitigation of free void-space and pinholes in the coatings. The hotplate was set at a temperature of 220–410 °C, which was verified using a handheld VWR High Temperature InfraRed Thermometer. Substrates were placed on the hotplate for 10 min and pre-equilibrated to temperatures of 390–410 °C prior to engaging the spray coating profile. The spray nozzle used had a diameter of 0.7112 cm and was set at a z-axis height of 12.065 cm, which yielded a spray cone with a diameter of 2.286 cm. The atomization pressure of 9.0 kPa was held constant across the experiments. The feed rate for PEI was maintained at 0.407 mL·min⁻¹. Feed rates for 1, 3, and 5 wt.% UFG/PEI dispersions were 0.477, 0.642, and 0.776 mL·min⁻¹, respectively. A total of 12–23 passes were applied depending on the feed rate, to yield pinhole-free coatings with thicknesses between 20–30 µm, as measured using a Dr. NIX Byko-Test 8500 Basic thickness meter.

Benchmark coating applications

Three Huntsman Araldite formulations (2011, 2013, and 2014) were acquired for comparison. Each type of epoxy was thinned using Sunnyside General Purpose, Professional Strength, Medium-Dry Lacquer Thinner in a 1:1 ratio, painted onto a surface-treated substrate, and allowed to cure overnight at room temperature. An aqueous dispersion of Dexnyl PEEK was mechanically shaken until all solid material settled to the bottom of the container and was then redispersed in the water to obtain a colloidal dispersion. The PEEK was then painted onto a cleaned and surface-treated AA 7075 substrate and cured in a Thermo Scientific Thermolyne benchtop muffle furnace at 420 °C for 10 min. Celazole IV PBI powder was dissolved in NMP at a concentration of 10 wt.%, and hand-sprayed using a TCP Global High Performance HVLP Spray Gun with a 1.4 mm tip at approximately 0.207 MPa on a hot plate set at 475 °C. The deposited film was then annealed at 250 °C for 5 min in the muffle furnace.

DC polarization measurements

A Gamry Potentiostat 1010E Interface was used for all electrochemical testing. All tests were performed in 3.5 wt.% aqueous solutions of NaCl. OCP measurements were acquired prior to each test where 1200 data points were acquired over a total time of 600 s in 0.5 s intervals. Potentiodynamic polarization (PDP) data was acquired in the range between -0.3 V and +0.3 V vs. E_{OC} at a scan rate of 1 mV·s⁻¹. Cyclic PDP was used to determine the pitting potential, repassivation potential, and to corroborate and/or deduce Tafel constants. Cyclic PDP was performed at an initial E(V) of -0.5 V vs. E_{OC} at a forward scan rate of 2 mV·s⁻¹, apex E(V) 1.5 vs. E_{OC} at a reverse scan rate of 2 mV·s⁻¹ vs. E_{OC}, and final E(V) 0.0 V vs. E_{OC} with apex / at 10 mA·cm⁻². Potentiostatic polarization (PSP) was used to determine the pitting stage at a final potential, which would generally yield pitting propagation in the 3.5 wt.% aqueous NaCl solution. The testing parameters were as follows: initial E(V) of 0.0 V vs. E_{OC}, initial time of 60 s, final E(V) of 0.3381 V vs. E_{REF}, and final time of 1200 s.

Electrochemical impedance spectroscopy (EIS)

EIS measurements were performed to examine the degradation of the coatings over the course of 100 days by immersing the coated substrates in an aerated 3.5 wt.% aqueous NaCl solution at room temperature. The electrochemical cell used a glass flange placed on top of an O-ring and clamped onto the coated substrate to create a working electrode with a surface area of 5.226 cm². A Ag/AgCl saturated calomel electrode (SCE) from Gamry served as the reference electrode with a Pt/Nb mesh counter electrode attached to a metal rod as the counter electrode. The electrochemical cell was placed within a Faraday cage. Each EIS measurement was preceded by an OCP measurement for 10 min, followed by potentiostatic impedance spectroscopy in the frequency range of 100 kHz to 10 mHz at ten points per decade and an amplitude of ±10 mV. Each test was repeated on duplicate substrates. The EIS data was fitted to equivalent circuit models using Gamry EChem Analyst and Pine Research AfterMath softwares.

ASTM adhesion testing

Three types of ASTM adhesion testing were performed, each of which utilized a standardized testing kit and parameters designated by ASTM guidelines. Tests performed included the ASTM D3359-17 tape test⁷⁶, the ASTM D4541-17 pull-off test⁷⁷, and the ASTM D2197-16 scrape test⁷⁸.

Cross-sectional imaging of coating/substrate interface

Cross-sectional SEM images were acquired for as-prepared and coated substrates after immersion in a 3.5 wt.% aqueous solution of NaCl. Changes in coating thickness, pitting propagation, and formation of an aluminum oxide layer were examined at the coating/metal interface by electron microscopy and energy dispersive X-ray mapping. Substrates with dimensions of 1.40 cm × 1.40 cm sections were cut and immersed in an EpoxiCure 2 epoxy resin and hardener mixed in a 4:1 (w/w) ratio and allowed to harden for 24 h. The sections were then sliced using a Buehler IsoMet diamond precision saw. One half of the sample was subsequently ground on a Buehler EcoMet 30 grinding/polishing wheel with 1200 grit P600, followed by a 4000 grit P1200 silicon carbide sandpaper. The sample was then polished using an Electron Microscopy Sciences 1 µm diamond polishing paste, diluted to 1 g·100 mL⁻¹ using Falcon Tool Company water-based polishing lubricant and diamond thinner, on 200 mm Struers MD-Floc polishing pads. Samples were then coated with 5 nm of Pt/Pd using a Ted Pella Cressington 108 Sputter Coater prior to imaging by SEM.

Field-emission SEM

SEM was performed on a JEOL JSM-7500F ultra-high-resolution field-emission instrument with a low-aberration conical objective lens, and a cold cathode UHV field-emission conical anode gun. SEM images were acquired at a working distance of 8 mm, accelerating voltage of 20.0 keV, an emission current of 20 μ A, and a probe current set at 12 nA \cdot cm $^{-2}$. An Oxford EDS system equipped with X-ray and digital imaging was used for elemental mapping.

Time-of-flight secondary ion mass spectrometry (ToF-SIMS)

ToF-SIMS was performed on a substrate coated with a ca. 20–30 μ m 5 wt.% UFG/PEI coating. A CAMECA IMS 4f ion microprobe was used to acquire a depth profile across the entire thickness of nanocomposite coating down to the coating/metal interface. The surface was sputtered using a 14.5 keV O $_2^+$ beam at a beam current of 0.3 μ A, beam diameter of 2 μ m, and a beam incidence angle of 26°. An initial raster scan was performed across a 100 μ m \times 100 μ m area. Two subsequent 50 μ m \times 50 μ m and 10 μ m \times 10 μ m areas raster scans were performed inside the first crater. A second ToF-SIMS experiment was performed on a ca. 5 μ m thick 5 wt.% UFG/PEI coating using a Tescan FERA-3 GMH Focused Ion Beam Microscope with an integrated Time-of-Flight Mass Spectrometer. This measurement obtained depth profile of the interface between the nanocomposite coating and the AA 7075 substrate. The surface was sputtered using a 30 keV Xe $^+$ beam with a current of 425 nA, beam diameter of <1 μ m, and incidence angle of 90°. An initial raster scan was performed across a 100 μ m \times 100 μ m area. Two further 80 μ m \times 80 μ m areas were sampled in the center of the first crater with a final depth of ca. 30 μ m.

Nanoindentation

Nanoindentation was performed using a commercial nanoindenter (Hysitron TI 950 Triboindenter) utilizing a Berkovich diamond indenter probe with a tip radius of 150 nm. The Oliver–Pharr model was used to analyze the collected data⁷⁹. To calculate the modulus of elasticity of the coatings, the Poisson's ratio of both the tip of the nanoindenter and the sample were considered as per:

$$E_r = \left(\frac{1 - \nu_i}{E_i} + \frac{1 - \nu_s}{E_s} \right)^{-1} \quad (1)$$

Where E_r is the reduced modulus, ν_i is Poisson's ratio for the indenter material, ν_s is Poisson's ratio for the sample material, E_i is Young's modulus for the indenter material, and E_s is Young's modulus for the sample material. For all the samples, a load of 4000 μ N was applied for 9 s, followed by a dwell time of 5 s, and unloading for 3 s. The maximum penetration depth was maintained below 10% of the nominal thickness of the coating to avoid substrate interactions. For each coating type, at least 36 indents were acquired in arrays of 3 \times 2 indents at six different locations. Standard deviations were calculated for the hardness and reduced modulus for all coating formulations.

X-Ray absorption near-edge structure (XANES) spectroscopy

XANES measurements were performed at the National Synchrotron Light Source II of Brookhaven National Laboratory beamline SST-1 operated by the National Institute of Standards and Technology. Measurements were performed in partial electron yield (PEY) mode with a nominal resolution of 0.1 eV. The PEY signal was normalized to the incident beam intensity of a clean gold grid to eliminate the effects of any incident beam fluctuations and optical absorption features. Three samples were compared: a control aluminum sample (Shepherd Starlight MicroMirror Technology aluminum flakes); ULTEM 1000 spray

coated onto a copper foil substrate, and a sample wherein Al flakes were blended with PEI and then spray-coated onto a copper foil substrate.

Inductively coupled plasma mass spectrometry (ICP-MS)

ICP-MS was performed on the corrosion electrolyte post-exposure to determine the concentration of dissolved Al using a PerkinElmer NExION300D instrument benchmarked to a Sc 45 internal standard. Samples were prepared for ICP-MS analyses by removing a 10 mL aliquot of the remaining 3.5 wt.% aqueous NaCl electrolyte solution after 100 days of exposure. The solution was then diluted with Milli-Q-purified H₂O until the estimated concentration of ions was in the detectable range. The measured concentration of metal ions has a relative uncertainty of 6.4%.

Received: 22 October 2022; Accepted: 31 March 2023;

Published online: 25 April 2023

REFERENCES

1. Bowman, E. et al. International measures of prevention, application, and economics of corrosion technologies study. *NACE Int.* **216**, 2–3 (2016).
2. Böhm, S. Graphene against corrosion. *Nat. Nanotechnol.* **9**, 741–742 (2014).
3. Birbilis, N., Choudhary, S., Scully, J. R. & Taheri, M. L. A perspective on corrosion of multi-principal element alloys. *NPJ Mater. Degrad.* **5**, 14 (2021).
4. Hou, B. et al. The cost of corrosion in China. *NPJ Mater. Degrad.* **1**, 4 (2017).
5. Hughes, A. E., Cole, I. S., Muster, T. H. & Varley, R. J. Designing green, self-healing coatings for metal protection. *NPG Asia Mater.* **2**, 143–151 (2010).
6. Verma, C., Ebenso, E. E., Quraishi, M. A. & Hussain, C. M. Recent developments in sustainable corrosion inhibitors: design, performance and industrial scale applications. *Mater. Adv.* **2**, 3806–3850 (2021).
7. Dennis, R. V. et al. Hybrid nanostructured coatings for corrosion protection of base metals: a sustainability perspective. *Mater. Res. Express* **2**, 032001 (2015).
8. Liu, M., Guo, Y., Wang, J. & Yergin, M. Corrosion avoidance in lightweight materials for automotive applications. *NPJ Mater. Degrad.* **2**, 24 (2018).
9. Honarvar Nazari, M. et al. Nanocomposite organic coatings for corrosion protection of metals: a review of recent advances. *Prog. Org. Coat.* **162**, 106573 (2022).
10. Othman, N. H. et al. Graphene-based polymer nanocomposites as barrier coatings for corrosion protection. *Prog. Org. Coat.* **135**, 82–99 (2019).
11. Davidson, R. D. et al. Tortuosity but not percolation: design of exfoliated graphite nanocomposite coatings for extended corrosion protection of aluminum alloys. *ACS Appl. Nano Mater.* **2**, 3100–3116 (2019).
12. Zhu, Y. et al. Ultrastrong nanotwinned titanium alloys through additive manufacturing. *Nat. Mater.* **21**, 1258–1262 (2022).
13. Pratap Singh, A., Gupta, A., Sai Jyothender, K. & Srivastava, C. Effect of Zn incorporation on the evolution of texture, strain, grain boundary constitution, and corrosion behavior of electrodeposited SnZn coatings. *Met. Mater. Trans. A* **53**, 2743–2753 (2022).
14. Milovanoff, A., Posen, I. D. & MacLean, H. L. Electrification of light-duty vehicle fleet alone will not meet mitigation targets. *Nat. Clim. Chang.* **10**, 1102–1107 (2020).
15. McCafferty, E. *Introduction to Corrosion Science* (Springer New York, 2010). <https://doi.org/10.1007/978-1-4419-0455-3>.
16. Maurice, V. & Marcus, P. Passive films at the nanoscale. *Electrochim. Acta* **84**, 129–138 (2012).
17. Fu, Y., Li, J., Luo, H., Du, C. & Li, X. Recent advances on environmental corrosion behavior and mechanism of high-entropy alloys. *J. Mater. Sci. Technol.* **80**, 217–233 (2021).
18. Marcus, P. Surface science approach of corrosion phenomena. *Electrochim. Acta* **43**, 109–118 (1998).
19. Marcus, P. On some fundamental factors in the effect of alloying elements on passivation of alloys. *Corros. Sci.* **36**, 2155–2158 (1994).
20. Long, R. S., Boettcher, E. & Crawford, D. Current and future uses of aluminum in the automotive industry. *JOM* **69**, 2635–2639 (2017).
21. Sadeghi, S. & Ebrahimifar, H. Effect of electrolyte pH on microstructure, corrosion behavior, and mechanical behavior of Ni-P-W-TiO₂ electroplated coatings. *J. Mater. Eng. Perform.* **30**, 2409–2421 (2021).
22. Hamza, H. M., Deen, K. M., Khaliq, A., Asselin, E. & Haider, W. Microstructural, corrosion and mechanical properties of additively manufactured alloys: a review. *Crit. Rev. Solid State Mater. Sci.* **47**, 1–53 (2021).

23. Abodi, L. C. et al. Modeling localized aluminum alloy corrosion in chloride solutions under non-equilibrium conditions: steps toward understanding pitting initiation. *Electrochim. Acta* **63**, 169–178 (2012).

24. Merten, B. J. E., Battocchi, D. & Bierwagen, G. P. Aluminum alloy 2024-T3 protection by magnesium-rich primer with chromate-free metal salts. *Prog. Org. Coat.* **78**, 446–454 (2015).

25. Dennis, R. V., Viyannalage, L. T., Aldinger, J. P., Rout, T. K. & Banerjee, S. Nanosstructured magnesium composite coatings for corrosion protection of low-alloy steels. *Ind. Eng. Chem. Res.* **53**, 18873–18883 (2014).

26. DeRosa, R. L., Szabo, I., Bierwagen, G. P. & Battocchi, D. The effect of exposure condition on the degradation behavior of magnesium rich coatings. *Prog. Org. Coat.* **78**, 455–461 (2015).

27. Davidson, R. D. et al. Magnesium nanocomposite coatings for protection of a lightweight al alloy: modes of corrosion protection. *Mechanisms Fail. Phys. status solidi (a)* **216**, 1800817 (2019).

28. Moshier, W. C., Davis, G. D., Ahearn, J. S. & Hough, H. F. Corrosion behavior of aluminum-molybdenum alloys in chloride solutions. *J. Electrochem. Soc.* **134**, 2677–2684 (1987).

29. Huttunen-Saarivirta, E., Vaganov, G. V., Yudin, V. E. & Vuorinen, J. Characterization and corrosion protection properties of epoxy powder coatings containing nanoclays. *Prog. Org. Coat.* **76**, 757–767 (2013).

30. Chen, Y. et al. Zinc phosphate coated modified hollow glass beads and their thermal insulation and anticorrosion performance in coatings. *Ceram. Int.* **47**, 23507–23517 (2021).

31. *Thermal Insulation Coating Market Share, Size, Trends, Industry Analysis Report, By Type (Acrylic, Epoxy, Polyurethane, Yttria Stabilized Zirconia); By End-Use (Manufacturing, Construction, Aerospace & Defense, Automotive); By Region; Segment Forecast, 20;* <https://www.polarismarketresearch.com/industry-analysis/thermal-insulation-coating-market> (2021).

32. Liu, G.-W. et al. Negative thermal expansion HfV_2O_7 nanostructures for alleviation of thermal stress in nanocomposite coatings. *ACS Appl. Mater. Interfaces* **13**, 44723–44732 (2021).

33. Shen, X., Wang, Z., Wu, Y., Liu, X. & Kim, J.-K. Effect of functionalization on thermal conductivities of graphene/epoxy composites. *Carbon* **108**, 412–422 (2016).

34. Xing, Z. et al. Investigation of the thermal conductivity of resin-based lightweight composites filled with hollow glass microspheres. *Polymers* **12**, 518 (2020).

35. O'Loughlin, T. E., Martens, S., Ren, S. R., McKay, P. & Banerjee, S. Orthogonal wettability of hierarchically textured metal meshes as a means of separating water/oil emulsions. *Adv. Eng. Mater.* **19**, 1600808 (2017).

36. O'Loughlin, T. E., Ngamassi, F.-E., McKay, P. & Banerjee, S. Separation of viscous oil emulsions using three-dimensional nanotrapodal ZnO membranes. *Energy Fuels* **32**, 4894–4902. (2018).

37. Schriver, M. et al. Graphene as a long-term metal oxidation barrier: worse than nothing. *ACS Nano* **7**, 5763–5768 (2013).

38. Zare, Y. & Rhee, K. Y. Development of a model for electrical conductivity of polymer/graphene nanocomposites assuming interphase and tunneling regions in conductive networks. *Ind. Eng. Chem. Res.* **56**, 9107–9115 (2017).

39. Terrones, M. et al. Interphases in graphene polymer-based nanocomposites: achievements and challenges. *Adv. Mater.* **23**, 5302–5310 (2011).

40. Jesson, D. A. & Watts, J. F. The interface and interphase in polymer matrix composites: effect on mechanical properties and methods for identification. *Polym. Rev.* **52**, 321–354 (2012).

41. Singh, S. & Srivastava, C. Effect of carbon nanotube incorporation on the evolution of morphology, phase and compositional homogeneity, surface oxide chemistry and corrosion behaviour of electrodeposited fecumnnico-carbon nanotube composite coatings. *Electrochim. Acta* **439**, 141693 (2023).

42. Cui, C., Lim, A. T. O. & Huang, J. A cautionary note on graphene anti-corrosion coatings. *Nat. Nanotechnol.* **12**, 834–835 (2017).

43. Guan, L.-Z. et al. Toward effective and tunable interphases in graphene oxide/epoxy composites by grafting different chain lengths of polyetheramine onto graphene oxide. *J. Mater. Chem. A Mater.* **2**, 15058 (2014).

44. Compton, O. C., Kim, S., Pierre, C., Torkelson, J. M. & Nguyen, S. T. Crumpled graphene nanosheets as highly effective barrier property enhancers. *Adv. Mater.* **22**, 4759–4763 (2010).

45. Zare, Y. & Rhee, K. Y. Modeling of interphase strength between polymer host and clay nanoparticles in nanocomposites by clay possessions and interfacial/interphase terms. *Appl. Clay Sci.* **192**, 105644 (2020).

46. Graedel, T. E. Corrosion mechanisms for aluminum exposed to the atmosphere. *J. Electrochem. Soc.* **136**, 204C–212C (1989).

47. Liu, Y. et al. Quantitative study of interface/interphase in epoxy/graphene-based nanocomposites by combining STEM and EELS. *ACS Appl. Mater. Interfaces* **8**, 34151–34158 (2016).

48. Moharana, S., Kar, S. K., Mishra, M. K., Mahaling, R. N. Synthesis and properties of graphene and graphene oxide-based polymer composites. *Surf. Eng. Graphene*, 175–201 (2019).

49. Voyiadjis, G. Z., Samadi-Dooki, A. & Malekmotie, L. Nanoindentation of high performance semicrystalline polymers: a case study on PEEK. *Polym. Test.* **61**, 57–64 (2017).

50. Iqbal, H. M. S., Bhowmik, S. & Benedictus, R. Performance evaluation of polybenzimidazole coating for aerospace application. *Prog. Org. Coat.* **105**, 190–199 (2017).

51. Yasin, G. et al. Synthesis of spheres-like Ni/Graphene nanocomposite as an efficient anti-corrosive coating: effect of graphene content on its morphology and mechanical properties. *J. Alloy. Compd.* **755**, 79–88 (2018).

52. Ren, Z. et al. Mechanical properties of nickel-graphene composites synthesized by electrochemical deposition. *Nanotechnol* **26**, 065706 (2015).

53. Khatam, H. & Ravi-Chandar, K. On the evaluation of the elastic modulus of soft materials using beams with unknown initial curvature. *Strain* **49**, 420–430 (2013).

54. Shi, X., Nguyen, T. A., Suo, Z., Liu, Y. & Avci, R. Effect of nanoparticles on the anticorrosion and mechanical properties of epoxy coating. *Surf. Coat. Technol.* **204**, 237–245 (2009).

55. Sinha Ray, S. & Okamoto, M. Polymer/layered silicate nanocomposites: a review from preparation to processing. *Prog. Polym. Sci.* **28**, 1539–1641 (2003).

56. Zare, Y., Rhee, K. Y. & Park, S. J. Predictions of micromechanics models for interfacial/interphase parameters in polymer/metal nanocomposites. *Int. J. Adhes. Adhes.* **79**, 111–116 (2017).

57. Desai, S. R., Wu, H., Rohlfing, C. M. & Wang, L.-S. A study of the structure and bonding of small aluminum oxide clusters by photoelectron spectroscopy: Al_xO_y ($x = 1–2$, $y = 1–5$). *J. Chem. Phys.* **106**, 1309–1317 (1997).

58. Li, H., Cheng, X. & Zhao, F. A study of Al_n ($n = 5, 6$) cluster bonding with some intermediate products of energetic materials. *Comput. Theor. Chem.* **1031**, 34–39 (2014).

59. Kim, K., Zhu, P., Li, N., Ma, X. & Chen, Y. Characterization of oxygen containing functional groups on carbon materials with oxygen K-Edge X-Ray absorption near edge structure spectroscopy. *Carbon N. Y.* **49**, 1745–1751 (2011).

60. Frati, F., Hunault, M. O. J. Y. & de Groot, F. M. F. Oxygen K-Edge X-Ray absorption spectra. *Chem. Rev.* **120**, 4056–4110 (2020).

61. Sainio, S. et al. Trends in carbon, oxygen, and nitrogen core in the x-ray absorption spectroscopy of carbon nanomaterials: a guide for the perplexed. *J. Phys. Chem. C* **125**, 973–988 (2021).

62. Dennis, R. V. et al. Near-Edge x-ray absorption fine structure spectroscopy study of nitrogen incorporation in chemically reduced graphene oxide. *J. VacSci. Tech. B* **31**, 041204 (2013).

63. Henderson, G. S., Neuville, D. R. & Cormier, L. An O K-Edge XANES study of glasses and crystals in the $\text{CaO}-\text{Al}_2\text{O}_3-\text{SiO}_2$ (CAS) system. *Chem. Geol.* **259**, 54–62 (2009).

64. Heymann, K., Lehmann, J., Solomon, D., Schmidt, M. W. I. & Rieger, T. C 1s K-Edge near Edge X-Ray absorption fine structure (NEXAFS) spectroscopy for characterizing functional group chemistry of black carbon. *Org. Geochem* **42**, 1055–1064 (2011).

65. Lee, V. et al. In situ near-Edge x-Ray absorption fine structure spectroscopy investigation of the thermal defunctionalization of graphene oxide. *J. Vac. Sci. Tech. B* **30**, 061206 (2012).

66. Grundmeier, G., Schmidt, W. & Stratmann, M. Corrosion protection by organic coatings: electrochemical mechanism and novel methods of investigation. *Electrochim. Acta* **45**, 2515–2533 (2000).

67. da Conceicao, T. F., Scharnagl, N., Dietzel, W. & Kainer, K. U. Corrosion protection of magnesium AZ31 alloy using poly(ether imide) [pei] coatings prepared by the dip coating method: influence of solvent and substrate pre-treatment. *Corros. Sci.* **53**, 338–346 (2011).

68. Lorenz, W. J. & Mansfeld, F. Determination of corrosion rates by electrochemical DC and AC methods. *Corros. Sci.* **21**, 647–672 (1981).

69. Jorcin, J.-B., Orazem, M. E., Pélère, N. & Tribollet, B. CPE analysis by local electrochemical impedance spectroscopy. *Electrochim. Acta* **51**, 1473–1479 (2006).

70. Macdonald, J. R. Impedance spectroscopy. *Ann. Biomed. Eng.* **20**, 289–305 (1992).

71. Orazem, M. E. & Tribollet, B. An integrated approach to electrochemical impedance spectroscopy. *Electrochim. Acta* **53**, 7360–7366 (2008).

72. Margarit-Mattos, I. C. P. EIS and organic coatings performance: revisiting some key points. *Electrochim. Acta* **354**, 136725 (2020).

73. MacDonald, M. A. & Andreas, H. A. Method for equivalent circuit determination for electrochemical impedance spectroscopy data of protein adsorption on solid surfaces. *Electrochim. Acta* **129**, 290–299 (2014).

74. McIntyre, J. M. & Pham, H. Q. Electrochemical impedance spectroscopy; a tool for organic coatings optimizations. *Prog. Org. Coat.* **27**, 201–207 (1996).

75. Wang, W., Juarez-Robles, D. & Mukherjee, P. P. Electroanalytical quantification of electrolyte transport resistance in porous electrodes. *J. Electrochem. Soc.* **167**, 080510 (2020).

76. ASTM. D3359-09: Standard test methods for measuring adhesion by tape test. *ASTM International*, No. Reapproved, 1–8. (2017).

77. ASTM. D4541-09: Standard test method for pull-off strength of coatings using portable adhesion. *ASTM International*, No. Reapproved, 1–16. (2017).

78. ASTM. D2197-16: Standard test method for adhesion of organic coatings by scrape adhesion. *ASTM International*, No. Reapproved, 1–4 (2017).
79. Oliver, W. C. & Pharr, G. M. An improved technique for determining hardness and elastic modulus using load and displacement sensing indentation experiments. *J. Mater. Res.* **7**, 1564–1583 (1992).

ACKNOWLEDGEMENTS

This project was funded by SABIC Specialties Inc. T.E.S. acknowledges the support of the NSF under a Graduate Research Fellowship grant DGE: 1746932. This research was supported by an appointment to the Intelligence Community Postdoctoral Research Fellowship Program at Texas A&M University administered by Oak Ridge Institute for Science and Education (ORISE) through an interagency agreement between the U.S. Department of Energy and the Office of the Director of National Intelligence (ODNI). W.Z. acknowledges the support from the Advanced Light Source (ALS) doctoral fellowship in residence. The Advanced Light Source is supported by the Director, Office of Science, Office of Basic Energy Sciences, U.S. Department of Energy under contract DE- AC02-05CH11231. Authors acknowledge the use of the TAMU Materials Characterization Facility (RRID:SCR_022202) and Dr. Yordanos Bisrat as well as Dr. Sisi Xiang. The authors acknowledge the assistance of the Texas A&M University Microscopy and Imaging Center Core Facility (RRID:SCR_022128).

AUTHOR CONTRIBUTIONS

T.E.S.: Conceptualization, Investigation, Data Curation, Methodology, Visualization, Formal Analysis, Writing – Original Draft. W.Z.: Conceptualization, Investigation. C.G.V., V.H.B., L.D., T.F.Jr., S.S.: Investigation. N.S.S.: Visualization, Validation, Software, Formal Analysis, Writing – Review & Editing. S.V.V.: Investigation, Data Curation, Formal Analysis. V.K., N.V.: Validation. M.P.: Data Curation, Validation. K.S.: Project Administration, Validation, Resources, Writing – Review & Editing. R.D.D.: Conceptualization, Project Administration, Supervision, Investigation, Visualization, Methodology, Writing – Review & Editing. S.B.: Conceptualization, Project Administration, Validation, Supervision, Writing – Review & Editing, Funding Acquisition.

COMPETING INTERESTS

The authors declare no competing interests.

ADDITIONAL INFORMATION

Supplementary information The online version contains supplementary material available at <https://doi.org/10.1038/s41529-023-00349-2>.

Correspondence and requests for materials should be addressed to Kapil Sheth, Rachel D. Davidson or Sarbjit Banerjee.

Reprints and permission information is available at <http://www.nature.com/reprints>

Publisher's note Springer Nature remains neutral with regard to jurisdictional claims in published maps and institutional affiliations.



Open Access This article is licensed under a Creative Commons Attribution 4.0 International License, which permits use, sharing, adaptation, distribution and reproduction in any medium or format, as long as you give appropriate credit to the original author(s) and the source, provide a link to the Creative Commons license, and indicate if changes were made. The images or other third party material in this article are included in the article's Creative Commons license, unless indicated otherwise in a credit line to the material. If material is not included in the article's Creative Commons license and your intended use is not permitted by statutory regulation or exceeds the permitted use, you will need to obtain permission directly from the copyright holder. To view a copy of this license, visit <http://creativecommons.org/licenses/by/4.0/>.

© The Author(s) 2023